Peculiar properties in quasinormal spectra from loop quantum gravity effect

Guoyang Fu,[1,2,5,†] Dan Zhang,[3,‡] Peng Liu,[4,§] Xiao-Mei Kuang,[2,‖] and Jian-Pin Wu[2,*]

[1]*Department of Physics and Astronomy, Shanghai Jiao Tong University, Shanghai 200240, China*
[2]*Center for Gravitation and Cosmology, College of Physical Science and Technology, Yangzhou University, Yangzhou 225009, China*
[3]*Department of Physics, Key Laboratory of Low-Dimensional Quantum Structures and Quantum Control of Ministry of Education, Synergetic Innovation Center for Quantum Effects and Applications, Hunan Normal University, Changsha, Hunan 410081, China*
[4]*Department of Physics and Siyuan Laboratory, Jinan University, Guangzhou 510632, People's Republic of China*
[5]*Shanghai Frontier Science Center for Gravitational Wave Detection, Shanghai Jiao Tong University, Shanghai 200240, China*

(Received 31 January 2023; accepted 27 December 2023; published 19 January 2024)

We investigate the quasinormal mode (QNM) spectra for scalar and electromagnetic fields over a covariant loop quantum gravity (LQG) black hole. For the fundamental modes, the LQG effect reduces the oscillations in the scalar field, however, it induces stronger oscillations in the electromagnetic field compared to the classical case. Under the scalar field perturbation, the system enjoys faster decaying modes with more oscillations than the electromagnetic field. Some peculiar phenomena emerge in the QNM spectra with higher overtones. A notable feature is the substantial divergence observed in the first several overtones from their Schwarzschild counterparts, with this discrepancy becoming magnified as the overtone number increases. Another remarkable phenomenon in higher overtones is that the quasinormal frequencies of the scalar field with $l = 0$ exhibit an oscillatory behavior as the quantum parameter r_0 increases significantly. These oscillations intensify with the rising overtone number. We hypothesize that this oscillatory pattern may be associated with the extremal effect.

DOI: 10.1103/PhysRevD.109.026010

I. INTRODUCTION

A nonperturbative and background-independent technique, loop quantum gravity (LQG) [1–4], provides a scenario for quantizing spacetime structure. This approach has been successfully applied to quantize symmetry reduced cosmological spacetimes, known as loop quantum cosmology (LQC) [5–12]. Effective LQC theory can be constructed by incorporating two key quantum gravity effects, namely, the inverse volume correction and the holonomy correction, which can be achieved using both the canonical approach [13–18] and the path integral perspectives [19–25]. The quantum gravity effects in LQC can be connected to low-energy physics, resulting in a solvable cosmological model for studying quantum gravity effects. In particular, the big bang singularity in classical general relativity (GR) is successfully avoided by the quantum gravity effects [5–12,26–31], which instead result in a nonsingular big bounce even at the semiclassical level [32,33].

Following the same idea in LQC [5–12], several effective black hole (BH) models with LQG corrections have been constructed. Up to date, most of the effective LQG-BHs are implemented through the input of the holonomy correction; see, for example, [34–44] and references therein. A common feature of LQG-BHs is that the singularity is replaced by a transition surface between a trapped and an antitrapped region, which can be understood as the interior region of black holes and white holes.

The heart of the holonomy correction is the phase space regularization technique called polymerization [45]. Because of this, the effective LQG-BH with holonomy correction is also known as the polymer BH. The basic idea behind polymerization is the replacement of the conjugate momentum p with their regularized counterpart $\sin(\bar{\lambda}p)/\bar{\lambda}$, where $\bar{\lambda}$ is a quantity known as the polymerization scale, which is linked to the area gap. Depending on whether the polymerization scale is a constant or phase-space-dependent function, the polymer BHs are classified into two basic types:

(i) μ_0-type scheme: In this scheme, the polymerization scale is assumed to remain constant over the whole

*Corresponding author: jianpinwu@yzu.edu.cn
†FuguoyangEDU@163.com
‡danzhanglnk@163.com
§phylp@email.jnu.edu.cn
‖xmeikuang@yzu.edu.cn

phase space [34–38]. This approach has the drawback that the final result is reliant on the fiducial structures, which are introduced in the construction of the classical phase space. In addition, even in the low-curvature regimes, significant quantum effects may manifest, making these models unphysical. To overcome this drawback, some generalized versions of the μ_0 scheme have been proposed (see, for example, [46–49]), which partially alleviate the issues mentioned above.

(ii) $\bar{\mu}$-type scheme: The polymerization scale in the $\bar{\mu}$-type scheme is chosen to be a function of the phase space [39–42] such that the dependency on fiducial structures is removed. Particularly, in the improved $\bar{\mu}$ scheme with Chiou's choice [40,41], the spacetime approaches sufficiently fast the Schwarzschild geometry at low curvatures, which cures the drawback of the μ_0 scheme [50–53].

Recently, following the idea of the anomaly-free polymerization in [54], a novel covariant model of a spherically symmetric BH with holonomy correction is proposed in [55,56]. The polymerization scale $\bar{\lambda}$ is a constant in this model, and it is related to a fundamental length scale r_0 by a constant of motion m. The resulting geometry corresponds to a singularity-free interior region and two asymptotically flat exterior regions of equal mass.

In this paper, we will mainly study the properties of the quasinormal modes (QNMs) of a probe scalar field and a probe Maxwell field over this covariant polymer BH. As we all know, during the ringdown phase of binary system coalescence, the BH emits the gravitational waves (GWs) with typical discrete frequencies, i.e., quasinormal frequencies (QNFs). According to [57], QNFs encode decaying scales and damped oscillating frequencies. Certainly, quantum effects have the imprints in the QNM spectra, which are expected to be detected in GW observations. Also, conversely, GW detection will serve as an important criterion for the correctness of candidate quantum gravity theories.

Our paper is organized as follows. In Sec. III, we present a brief discussion on the effective potentials of scalar and Maxwell fields over the covariant LQG-BH. Section IV is dedicated to the properties of the QNM spectra. Then, we further study the ringdown waveform in Sec. V. We present the conclusions and discussions in Sec. VI. Appendixes A and B present a detailed derivation of the wave equations and the QNMs in the eikonal limit.

II. EFFECTIVE QUANTUM-CORRECTED SCHWARZSCHILD GEOMETRY

In Refs. [55,56], the authors proposed a novel effective LQG-corrected spherically symmetric black hole model with holonomy corrections that is covariant. In this section, we will present a brief review of this model.

A. Effective quantum-corrected Schwarzschild geometry

In the framework of canonical GR depicted by the Ashtekar-Barbero variables, a spherically symmetric model can be fully characterized by four dynamic variables: the two independent components of a desensitized triad $\tilde{E}^x$ and $\tilde{E}^\varphi$, along with their corresponding conjugate momenta $\tilde{K}_x$ and $\tilde{K}_\varphi$. In this context, x signifies the radial direction, while φ represents the azimuthal angle. When incorporating holonomy corrections, the following canonical transformation is employed, as detailed in [55,56]:

$$\tilde{E}^x \to E^x, \qquad \tilde{K}_x \to K_x, \qquad \tilde{E}^\varphi \to \frac{E^\varphi}{\cos(\bar{\lambda}K_\varphi)},$$
$$\tilde{K}_\varphi \to \frac{\sin(\bar{\lambda}K_\varphi)}{\bar{\lambda}}. \tag{1}$$

The parameter $\bar{\lambda}$, which can be conveniently taken as positive without loss of generality, is a dimensionless parameter inspired by holonomies. Notably, as $\bar{\lambda}$ approaches zero, the transformation is the identity, representing the limit where GR is recovered.

Under the transformation (1), the diffeomorphism constraint remains unchanged, represented as

$$\mathcal{D} = -E^{x\prime}K_x + E^\varphi K'_\varphi, \tag{2}$$

where the prime denotes the derivative with respect to x. However, to ensure an algebra free of anomalies, it is necessary to perform a linear combination between the Hamiltonian constraint and the diffeomorphism constraint, as discussed in [54]. In addition, we also need regularize the poles $\cos(\bar{\lambda}K_\varphi) = 0$. Taking these considerations into account, a deformed Hamiltonian constraint can be constructed as [55,56]

$$\begin{aligned}\mathcal{H} = &-\frac{E^\varphi}{2\sqrt{E^x}\sqrt{1+\bar{\lambda}^2}}\left(1+\frac{\sin^2(\bar{\lambda}K_\varphi)}{\bar{\lambda}^2}\right)\\ &-\sqrt{E^x}K_x\frac{\sin(2\bar{\lambda}K_\varphi)}{\bar{\lambda}\sqrt{1+\bar{\lambda}^2}}\left(1+\left(\frac{\bar{\lambda}E^{x\prime}}{2E^\varphi}\right)^2\right)\\ &+\frac{\cos^2(\bar{\lambda}K_\varphi)}{2\sqrt{1+\bar{\lambda}^2}}\left(\frac{E^{x\prime}}{2E^\varphi}(\sqrt{E^x})'+\sqrt{E^x}\left(\frac{E^{x\prime}}{E^\varphi}\right)'\right),\end{aligned} \tag{3}$$

along with its smeared form $H[f] \coloneqq \int f\mathcal{H}dx$. For more comprehensive details, please refer to [55,56].

By solving the system's equations of motion, which are derived from the Poisson brackets of various variables with the Hamiltonian, we can obtain the following explicitly

spherically symmetric metric:

$$ds^2 = -N(t,x)^2dt^2 + \left(1 - \frac{r_0}{\sqrt{E^x(t,x)}}\right)^{-1}\frac{E^\varphi(t,x)^2}{E^x(t,x)} \times (dx + N^x(t,x)dt)^2 + E^x(t,x)d\Omega^2, \quad (4)$$

where N and N^x represent the lapse and shift functions, respectively. The parameter r_0 represents a new length scale and is determined by the expression

$$r_0 = 2m\frac{\bar{\lambda}^2}{1+\bar{\lambda}^2}, \quad (5)$$

where m stands as a constant of motion. Notably, the length scale r_0 sets a minimum area r_0^2 for this model [55,56]. In contrast to its classical counterpart, it incorporates the term $1 - r_0/\sqrt{E^x}$.

We would like to emphasize that different gauge choices will result in distinct charts and their corresponding line elements for the same metric, ultimately yielding a consistent spacetime solution. The region containing the BH along with an asymptotically flat region can be described using the coordinate system $t, x = t, r$, in conjunction with the spherical metric θ, φ. This quantum-corrected spacetime also possesses a maximal analytical extension [55,56], as depicted in the Penrose diagram shown in Fig. 1. In this diagram:

(i) Region I corresponds to the asymptotically flat region with $r \in (r_h, \infty)$. This region includes the usual conformal infinities, namely, the timelike infinities denoted as i^- and i^+, the null infinities referred to as $\mathcal{J}^-$ and $\mathcal{J}^+$, and the spatial infinity marked as i^0.

(ii) Region II is the BH region with $r \in (r_0, r_h)$. It is evident that the hypersurface $r = r_0$ is a transition surface between the BH and the white hole (WH) regions.

(iii) Regions III and IV are regions that cannot be covered by the coordinate system (t, r, θ, φ); they correspond to the WH region and another asymptotically flat region, respectively.

The regions with dashed contours at the bottom and top are duplicates of the structure in the middle.

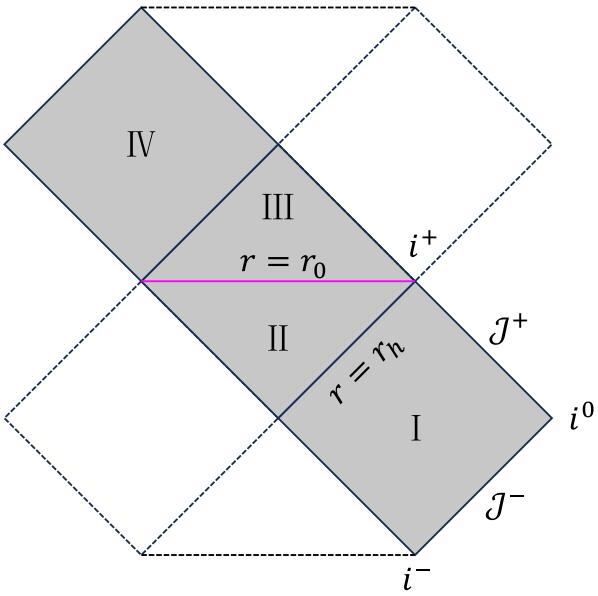

FIG. 1. Penrose diagram with maximal analytical extension of the quantum-corrected spacetime.

In this paper, our primary focus is the study of the QNMs for the BH part, thus limiting our attention to the exterior region of this quantum-corrected spacetime, as described by the following metric [55,56]:

$$ds^2 = -f(r)dt^2 + \frac{1}{g(r)f(r)}dr^2 + r^2d\Omega^2,$$
$$f(r) = 1 - \frac{2m}{r}, \qquad g(r) = 1 - \frac{r_0}{r}, \quad (6)$$

where $r \in (r_h, \infty)$ with $r_h = 2m$. Notably, in the limit as $\bar{\lambda} \to 0$, this new length scale tends to zero, i.e., $r_0 = 0$, thereby restoring the classical Schwarzschild (SS) BH. Furthermore, as we move to the low-curvature regions, the quantum gravity effects die off.

B. Mass and energy

This section provides a concise overview of the typical geometric definitions of mass and energy applied to this solution. This discussion aids in gaining a thorough understanding of the model's parameters. A straightforward calculation reveals that the Komar mass is a function of r and is expressed as follows [56]:

$$M_K(r) = m\sqrt{1 - \frac{r_0}{r}}. \quad (7)$$

It is readily apparent that the Komar mass approaches the constant of motion m as it tends to infinity. The dependence of the Komar mass on r is a consequence of the nonzero Ricci tensor.

The Hawking mass, equivalently, the Misner-Sharp mass, also exhibits a dependence on r and can be expressed as follows [56]:

$$M_H(r) = m + \frac{r_0}{2} - \frac{mr_0}{r}. \quad (8)$$

This quantity is consistently positive and, notably, coincides with m solely at the horizon. It is evident that the presence of a nonzero Ricci tensor exerts distinct influences on the Komar and Hawking masses.

Another important quantity is the Arnowitt-Deser-Misner (ADM) mass. The ADM mass on the hypersurfaces Σ_t can be worked out as follows [55,56]:

$$M^t_{\mathrm{ADM}} = m + \frac{r_0}{2}. \tag{9}$$

It is evident that the ADM mass is a geometric invariant and converges to the Hawking mass in the limit of infinity; whereas the ADM mass on any hypersurface Σ_τ is given by

$$M^\tau_{\mathrm{ADM}} = \frac{r_0}{2}. \tag{10}$$

This result is characterized by the parameter r_0 and recovers the one in the GR limit.

Additionally, we can calculate the Geroch energy. It is noteworthy that the Geroch energy on the hypersurface Σ_t is found to coincide with the Hawking energy. Meanwhile, the Geroch energy on Σ_τ equals the ADM mass of Σ_τ, as expressed by

$$E^\tau_G(r) = \frac{r_0}{2}. \tag{11}$$

An important point to highlight is that the Geroch mass is a quasilocal quantity.

We are also interested in the surface gravity κ, which is given by

$$\kappa = \frac{1}{4m}\sqrt{1 - \frac{r_0}{2m}}. \tag{12}$$

This fulfills the typical relation $|\kappa| = r^{-2}M_K|_{r=2m}$. It is worth noting that, in the limit where $r_0 \to 2m$, the surface gravity becomes zero, akin to the extremal Reissner-Nordström spacetime. The existence of a minimum area results in the surface gravity being smaller than that of a Schwarzschild BH with mass m.

III. SCALAR AND MAXWELL FIELDS OVER THE LQG-BH

We focus on the perturbations of the massless scalar field Φ and electromagnetic field A_μ over this LQG black hole and study their response. Notice that, in the following, we shall set $m = 1/2$ without loss of generality, which leads to the horizon located at $r_h = 1$. We write down the covariant equations for the test scalar field and electromagnetic field as follows:

$$\frac{1}{\sqrt{-g}}(g^{\mu\nu}\sqrt{-g}\Phi_\mu)_{,\nu} = 0, \tag{13}$$

$$\frac{1}{\sqrt{-g}}(g^{\alpha\mu}g^{\sigma\nu}\sqrt{-g}F_{\alpha\sigma})_{,\nu} = 0, \tag{14}$$

where $F_{\alpha\sigma} = \partial_\alpha A_\sigma - \partial_\sigma A_\alpha$ is the field strength of the Maxwell field. After the separation of variables, the aforementioned equations can be packaged into the Schrödinger-like form (for more details, see Appendix A),

$$\frac{\partial^2\Psi}{\partial r_*^2} + (\omega^2 - V_{\mathrm{eff}})\Psi = 0, \tag{15}$$

where r_* is the tortoise coordinate and V_{eff} is the effective potential,

$$V_{\mathrm{eff}} = f(r)\frac{l(l+1)}{r^2} + \frac{1-s}{r}\frac{d}{dr_*}f(r)\sqrt{g(r)}, \tag{16}$$

with l being the angular quantum numbers. $s = 0$ and $s = 1$ correspond to the scalar field and electromagnetic field, respectively. Figures 2 and 3 demonstrate the effective potentials as a function of r_* for scalar and electromagnetic fields with different l and r_0. It is found that both effective potentials are positive, indicating the LQG black hole is stable under scalar and electromagnetic perturbations. Furthermore, we would like to compare the differences in effective potentials between scalar and electromagnetic

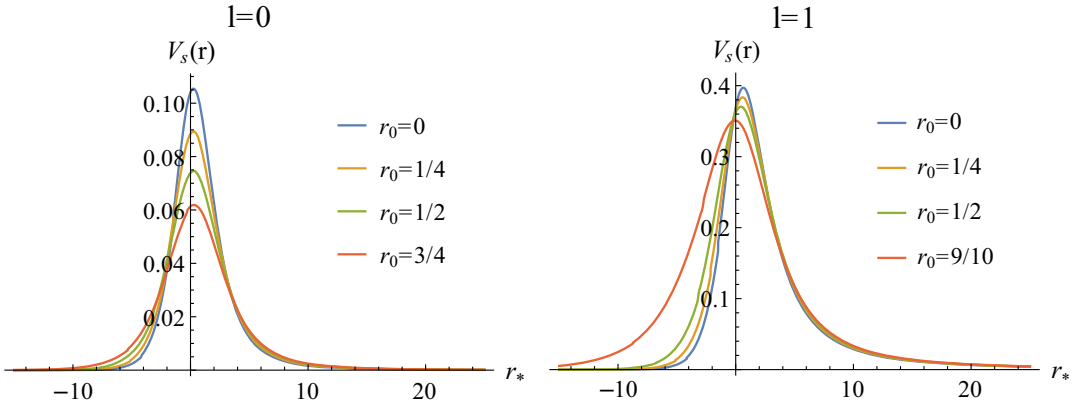

FIG. 2. The effective potentials $V_s(r_*)$ of the scalar field for different r_0 with fixed l.

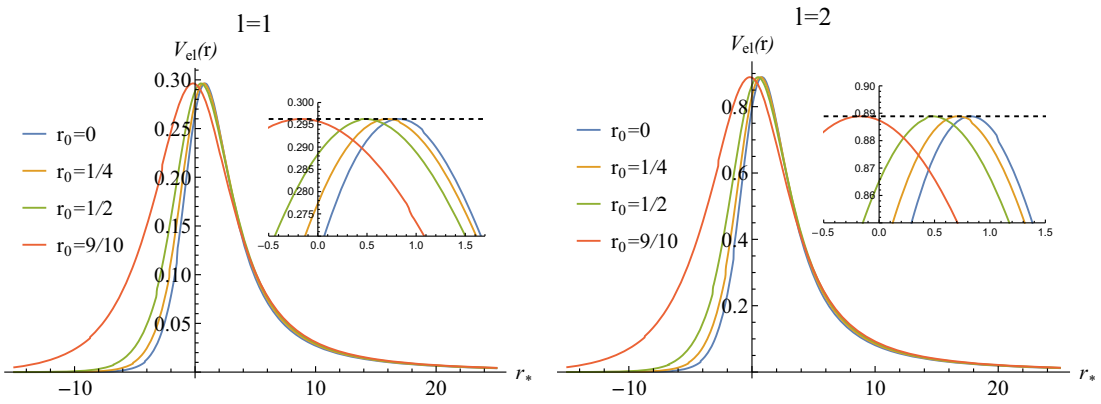

FIG. 3. The effective potentials $V_{el}(r_*)$ of the electromagnetic field for different r_0 with fixed l.

fields. It is easy to find that, for the electromagnetic field ($s = 1$), the second term in Eq. (16) vanishes, such that all the peaks of the effective potentials V_{el} have the same height for different r_0 (see Fig. 3). However, for the scalar field, i.e., $s = 0$, the second term in Eq. (16) survives and the height of the effective potential V_s depends on r_0. In particular, with increasing r_0, the height of V_s decreases (Fig. 2). The shape of the effective potentials shall definitely result in different properties of the QNMs.

IV. QUASINORMAL MODES

In this section, we investigate the QNMs spectra and specially focus on the effects from quantum gravity corrections. The nature of determining the QNMs is to solve the eigenvalue problem. To this end, we will impose a purely outgoing wave at infinity and purely ingoing wave at the horizon as follows:

$$\begin{aligned} &\text{horizon}: \partial_t\Psi - \partial_{r_*}\Psi = 0, \\ &\text{infinity}: \partial_t\Psi + \partial_{r_*}\Psi = 0. \end{aligned} \tag{17}$$

By solving Eq. (15) with the aforementioned boundary conditions, numerous techniques have been developed to determine the QNMs spectra, such as the Wentzel-Kramers-Brillouin (WKB) method [58–63], Horowitz-Hubeny method [64], continued fraction method [65], asymptotic iteration method [66–68], pseudospectral method [69,70], and so on. In this paper, we will solve the eigenvalue problem using the pseudospectral method. For more applications of the pseudospectral method in determining the QNMs in black hole physics, we can refer the reader to [71–80] and references therein. It is convenient to work in the Eddington-Finkelstein coordinate, which makes the wave equation (15) linear in the frequency. To achieve this goal, it is direct to make a transformation as

$$r \to 1/u \quad \text{and} \quad \Psi = e^{-i\omega r_*(u)}\psi. \tag{18}$$

Then, the wave equation (15) turns into the following form:

$$\begin{aligned} &\psi''(u) + \left(\frac{f'(u)}{f(u)} + \frac{g'(u)}{2g(u)} + \frac{2i\omega}{u^2 f(u)\sqrt{g(u)}}\right)\psi'(u) \\ &-\frac{1}{u}\left(\frac{2i\omega}{u^2 f(u)\sqrt{g(u)}} + \frac{V_{\text{eff}}(u)}{u^3 f(u)^2 g(u)} + \frac{f'(u)}{f(u)} + \frac{g'(u)}{2g(u)}\right) \\ &\times \psi(u) = 0. \end{aligned} \tag{19}$$

Combined with the boundary conditions (17), one can solve Eq. (19) by the pseudospectral method.

Now, we evaluate the QNM spectra for various values of the free parameter r_0 to explore the LQG effects on these spectra, as well as the differences between them and those of the Schwarzschild BH ($r_0 = 0$). Figures 4 and 5 show the QNFs as functions of r_0 for both the scalar field and electromagnetic field, respectively, showcasing multiple overtone numbers. We also provide the values of the QNFs for some specific parameter r_0 in Tables I–IV. We first summarize the properties of the fundamental modes ($n = 0$) as follows.

(i) For the scalar field, the real parts of the QNF, Reω decreases with increasing r_0 (left plots in Fig. 4). This means that the LQG effect reduces the oscillations in comparison to the Schwarzschild black hole. By contrast, Reω of the electromagnetic field exhibits an inverse tendency. That is, when r_0 increases, so does Reω. As a result, the LQG effect produces stronger oscillations in the electromagnetic field than that of the Schwarzschild black hole.

(ii) Whether for the scalar or electromagnetic field, the imaginary part of QNF Imω always lives in the lower half-plane, and their absolute values are less than that of the Schwarzschild black hole. Therefore, the system is stable in the presence of scalar or electromagnetic field perturbations, and the LQG effect results in slower decaying modes.

(iii) When we fix r_0, the scalar field has larger absolute values of Reω or Imω than the electromagnetic field (see Figs. 4 and 5). This indicates that, in

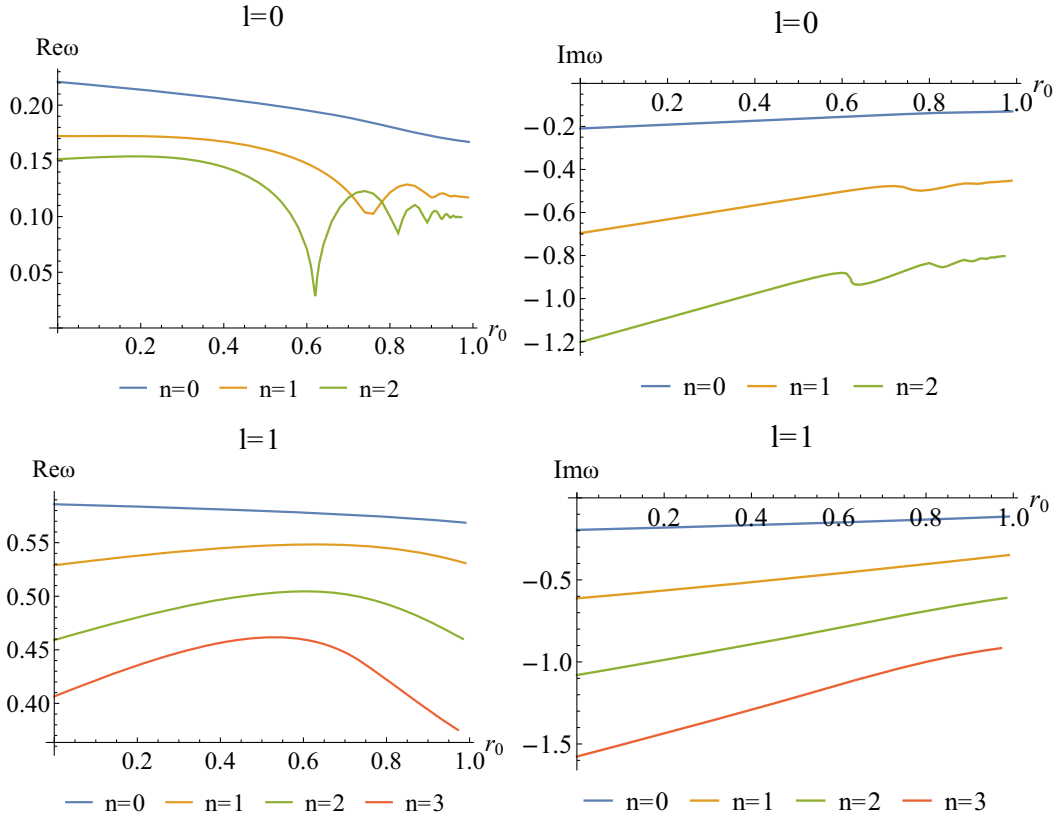

FIG. 4. QNFs as a function of r_0 for the scalar field perturbation.

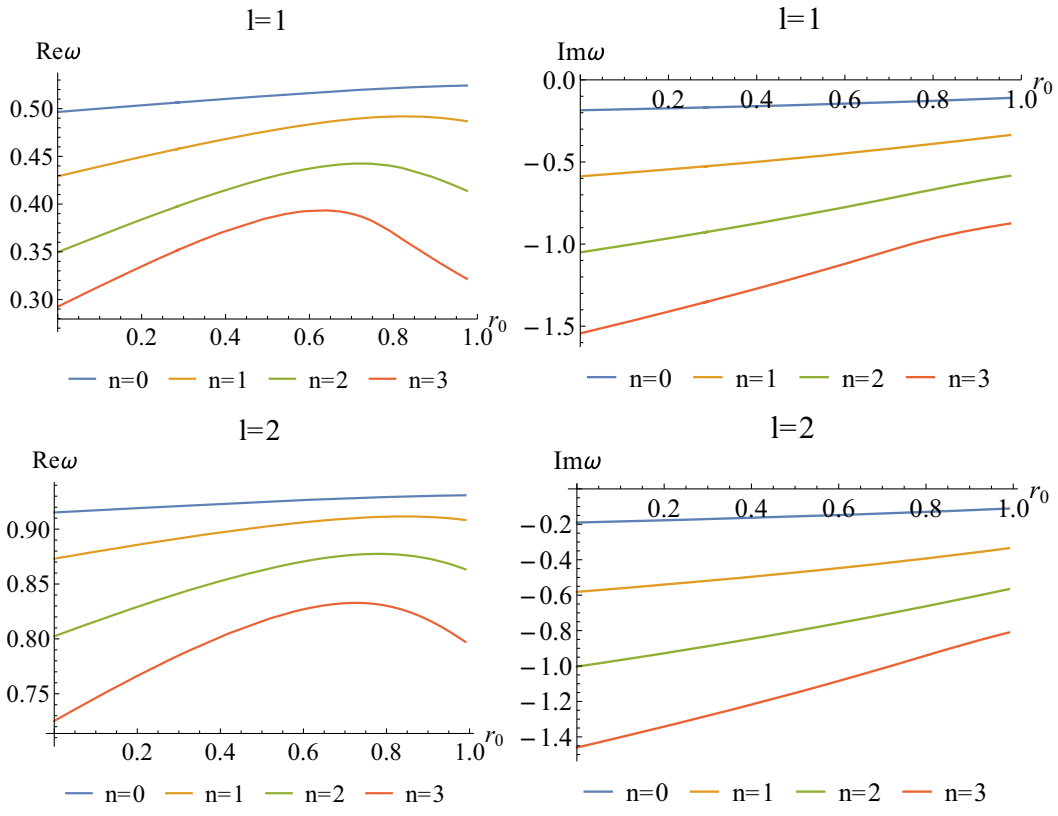

FIG. 5. QNFs as a function of r_0 for the electromagnetic field perturbation.

TABLE I. The QNM spectra for the scalar field perturbation for $l = 0$ with different n and r_0.

n	ω ($r_0 = 0$)	ω ($r_0 = 1/100$)	ω ($r_0 = 1/2$)	ω ($r_0 = 9/10$)
0	0.220910–0.209792i	0.220578–0.208911i	0.200799–0.164527i	0.172186–0.133779i
1	0.172223–0.696106i	0.172273–0.692920i	0.160438–0.534669i	0.117132–0.465373i
2	0.151564–1.202642i	0.151650–1.196552i	0.126266–0.921455i	0.102060–0.826914i
3	0.142272–1.705216i	0.141476–1.699571i	0.076951–1.314823i	0.098727–1.175255i
4	0.134739–2.211987i	0.133115–2.201015i	0.053109–1.808749i	0.094052–1.519302i
5	0.129639–2.712112i	0.129003–2.704325i	0.098367–2.213623i	0.083108–1.869088i

TABLE II. The QNM spectra for the scalar field perturbation for $l = 1$ with different n and r_0.

n	ω ($r_0 = 0$)	ω ($r_0 = 1/100$)	ω ($r_0 = 1/2$)	ω ($r_0 = 9/10$)
0	0.585872–0.195320i	0.585765–0.194632i	0.579649–0.158265i	0.571522–0.122834i
1	0.528897–0.612515i	0.529378–0.610151i	0.547089–0.487735i	0.539232–0.374106i
2	0.459079–1.080267i	0.460200–1.075690i	0.502191–0.843179i	0.476752–0.643355i
3	0.406517–1.576596i	0.408055–1.569596i	0.461392–1.216781i	0.394074–0.946941i
4	0.370218–2.081524i	0.372040–2.072076i	0.426854–1.597881i	0.317781–1.289254i
5	0.344154–2.588236i	0.346193–2.576352i	0.395550–1.981462i	0.263692–1.650819i

TABLE III. The QNM spectra for the electromagnetic field perturbation for $l = 1$ with different system parameters n and r_0.

n	ω ($r_0 = 0$)	ω ($r_0 = 1/100$)	ω ($r_0 = 1/2$)	ω ($r_0 = 9/10$)
0	0.496527–0.184975i	0.496879–0.184421i	0.513377–0.152855i	0.523384–0.117771i
1	0.429031–0.587335i	0.430079–0.585304i	0.476434–0.474099i	0.490764–0.358757i
2	0.349547–1.050375i	0.351295–1.046207i	0.427459–0.825862i	0.427304–0.616791i
3	0.292353–1.543818i	0.294508–1.537311i	0.385422–1.197325i	0.341172–0.908634i
4	0.253105–2.045090i	0.255501–2.036119i	0.351646–1.576036i	0.259632–1.241057i
5	0.224562–2.547950i	0.227824–2.536499i	0.322640–1.956797i	0.199813–1.593456i

TABLE IV. The QNM spectra for the electromagnetic field perturbation for $l = 2$ with different system parameters n and r_0.

n	ω ($r_0 = 0$)	ω ($r_0 = 1/100$)	ω ($r_0 = 1/2$)	ω ($r_0 = 9/10$)
0	0.915191–0.190009i	0.915392–0.189392i	0.924716–0.155637i	0.930332–0.120325i
1	0.873085–0.581420i	0.873735–0.579444i	0.901934–0.472399i	0.911143–0.362898i
2	0.802373–1.003175i	0.803766–0.999483i	0.862549–0.803573i	0.873233–0.611234i
3	0.725190–1.460397i	0.727327–1.454593i	0.816205–1.152343i	0.817382–0.869439i
4	0.657473–1.943219i	0.660188–1.935080i	0.770903–1.515796i	0.745134–1.142754i
5	0.602986–2.439431i	0.606126–2.428886i	0.730157–1.888692i	0.661207–1.437692i

comparison to the electromagnetic field, the system under scalar field perturbation enjoys faster decaying modes with greater oscillations.

Next, we delve into an investigation of the properties of the QNM spectra with higher overtones. It is found that higher overtones exhibit some peculiar properties, differing significantly from those of the fundamental modes. We will now summarize their key properties.

(i) For both the scalar field and the electromagnetic field, the first several overtones exhibit a substantially higher rate of deviation from their Schwarzschild values when compared to the fundamental mode, and this deviation rate increases with the overtone number (see Figs. 4 and 5, as well as Tables I–IV). Especially, for the scalar field with $l = 0$, the real oscillation frequency of the second overtone falls by more than 6 times its Schwarzschild limit, but the fundamental mode just slightly changes. This emergence of the outburst of overtones can be attributed to differences in the region

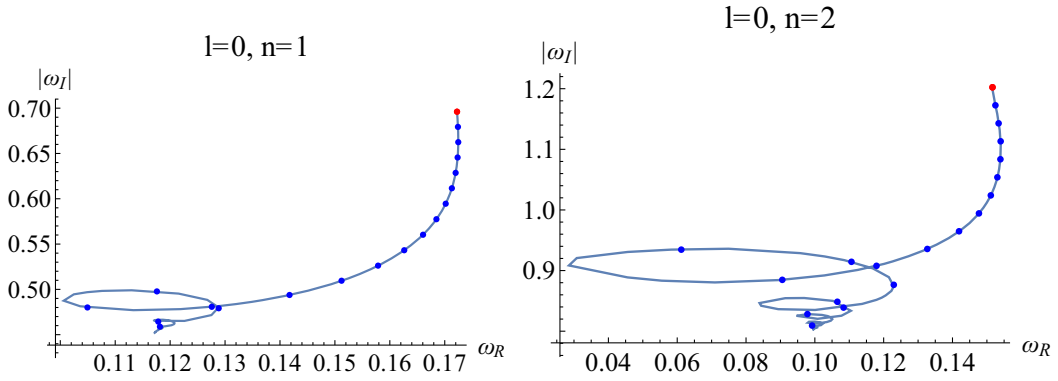

FIG. 6. QNFs of the scalar field perturbation with $n = 1$ (left) and $n = 2$ (right) for r_0 range from 0 to 0.99. The red points represent the $r_0 = 0$ (SS-BH) and the blue points correspond to $19r_0 = 1, 2, \ldots, 18$.

near the event horizon between the Schwarzschild BH and the LQG-corrected BH (see Figs. 2 and 3). Similar phenomena have been observed in alternative geometries beyond the Schwarzschild BH, including the Reissner-Nordström BH, Bardeen BH, and the higher-derivative gravity model [81–86].

(ii) A remarkable phenomenon is seen wherein the QNFs of the scalar field with $l = 0$ exhibit an oscillatory behavior when the quantum parameter r_0 increases significantly for higher overtones. The oscillations intensify with an increase in the overtone number. Similar oscillatory behaviors are also observed in Reissner-Nordström and Kerr BHs when these BHs approach the extremal case, as noted in [81]. We hypothesize that this oscillatory behavior may be linked to the extremal effect and, as such, warrants further investigation. Additionally, we suspect that similar oscillatory patterns may emerge in the case of a scalar field with high l and in the context of the electromagnetic field when the overtone number is sufficiently high. Unfortunately, our current numerical techniques constrain us from calculating QNFs for higher overtone numbers at this time. We hope to address this issue in the near future.

(iii) In Fig. 6, the phase diagram $\omega_R - |\omega_I|$ is presented. The trajectory depicted in the phase diagram diverges from the Schwarzschild QNMs and spirals toward a stable point. This discovery aligns with the findings in [87]. This phenomenon actually reflects the previously mentioned oscillatory behavior and has also been observed in the context of the Reissner-Nordström and Kerr BHs [81,88].

Finally, we will discuss the properties of the QNMs in the eikonal limit ($l \to \infty$). In [89], Cardoso *et al.* have demonstrated that, in the eikonal limit, QNMs may be connected with the behavior of null particles trapped on the unstable circular geodesic of the spacetime, which have been validated in most static, spherically symmetric, asymptotically flat spacetime. The Reω is determined by the angular velocity Ω_c at the unstable null geodesic [90–94], whereas the Imω is connected to the Lyapunov exponent λ [95,96]. In the LQG-BH background, we can calculate the QNMs in the eikonal limit, which is given by

$$\omega = \Omega_c l - i\left(n + \frac{1}{2}\right)|\lambda|. \tag{20}$$

For the detailed calculation, we can refer to Appendix B. It is found that, as SS-BH, the angular velocity Ω_c is completely determined by the black hole mass,

$$\Omega_c = \frac{1}{3\sqrt{3}m}. \tag{21}$$

Therefore, the Reω is independent of the LQG parameter r_0. While the Lyapunov exponent λ is given by

$$\lambda = \sqrt{-\frac{r_c^2}{f(r_c)}\left(\frac{d^2}{dr_*^2}\frac{f(r)}{r^2}\right)\Big|_{r=rc}}, \tag{22}$$

where r_c is the radius of the photon sphere. Obviously, the Lyapunov exponent is affected by the LQG correction. The left plot in Fig. 7 shows the Lyapunov exponent λ as a function of r_0. We see that the Lyapunov exponent decreases with r_0 increasing. Correspondingly, the absolution value of Imω is suppressed by the LQG effect (see the right plot in Fig. 7).

We notice that since the real part of QNF is independent of the LQG parameter r_0 in the eikonal limit, we expect that, as l increases, the difference in Reω between the LQG-BH and SS-BH will be suppressed and vanish. Figure 8 validates the argument that, as l increases, the difference rapidly decreases and goes to zero.

V. RINGDOWN WAVEFORM

In this section, we will study the time evolution of the scalar and electromagnetic perturbations, which help us to further know the total contributions from overtones. Here,

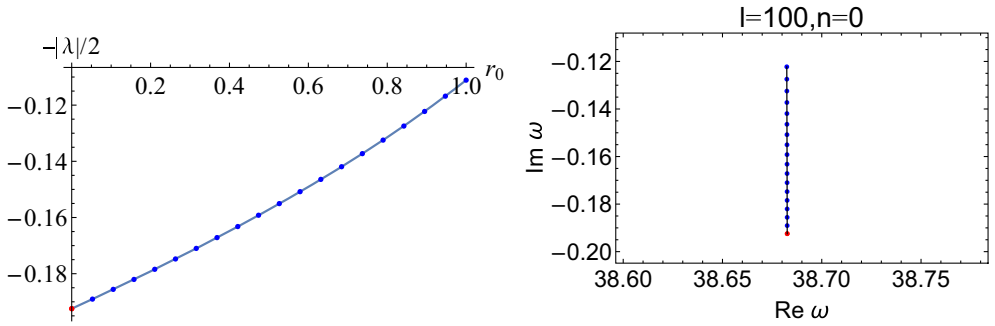

FIG. 7. Left: the Lyapunov exponent λ as a function of the LQG-corrected parameter r_0. Right: the QNFs for different r_0 for large l. The red points represent the $r_0 = 0$ (SS-BH) and the blue points correspond to $19r_0 = 1, 2, \ldots, 18$.

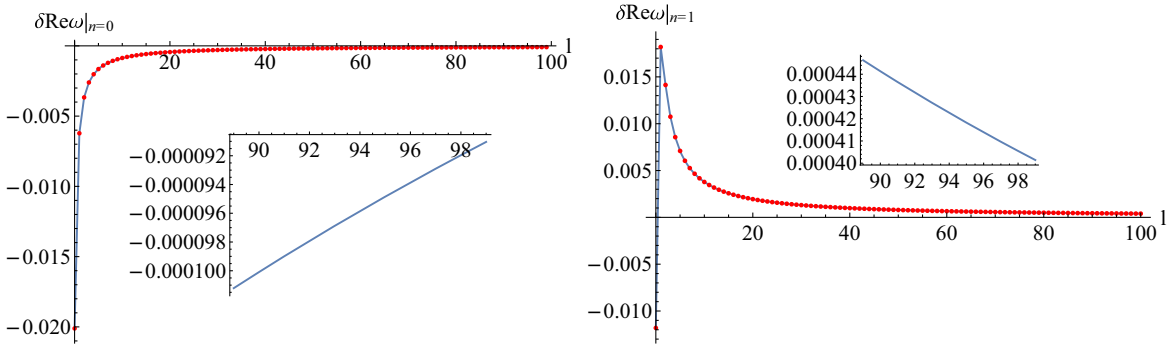

FIG. 8. The difference of QNFs of scalar field with $r_0 = 1/2$ between the LQG-BH and SS-BH. Left: $n = 0$. Right: $n = 1$.

we will use the finite difference method (FDM) technique to implement the dynamical evolution. For more details on the FDM, refer to Refs. [73,97–100] and references therein. To this end, we write the wave equation in difference form as

$$-\frac{(\Psi_{i+1,j}-2\Psi_{i,j}+\Psi_{i-1,j})}{\triangle t^2}+\frac{(\Psi_{i,j+1}-2\Psi_{i,j}+\Psi_{i,j-1})}{\triangle r_*^2} - V_j\Psi_{i,j}+\mathcal{O}(\triangle t^2)+\mathcal{O}(\triangle r_*^2)=0, \tag{23}$$

where $\triangle t$ and $\triangle r_*$ are the time and radial intervals, respectively, which are defined by $t = i\triangle t$ and $r_* = j\triangle r_*$. The V_j is the discrete form of the effective potential (16). Then, the iterate formula is derived as

$$\Psi_{i+1,j} = -\Psi_{i-1,j}+\frac{\triangle t^2}{\triangle r_*^2}(\Psi_{i,j+1}+\Psi_{i,j-1}) + \left(2-2\frac{\triangle t^2}{\triangle r_*^2}-\triangle t^2 V_j\right)\Psi_{i,j}. \tag{24}$$

Notice that the Courant-Friedrichs-Lewy condition for instability requires that $\triangle t/\triangle r_* < 1$. Using the iterate formula (24) with the initial Gaussian distribution $\Psi(r_*, t < 0) = 0$ and $\Psi(r_*, t = 0) = \exp -\frac{(r_*-a)^2}{2b^2}$, one can obtain the ringdown profiles.

In general, there are three different stages in time-evolution profile: initial outburst, quasinormal ringing, which depends only on the black hole's characteristics and is very important for GW observations [57,101–103], and the late tail, which exhibits the power-law behavior for the asymptotically flat spacetimes or exponential behavior for asymptotically de Sitter spacetimes. We will focus on the properties of the latter two stages in this section.

Figures 9 and 10 display the time-domain profile for both the scalar field and the electromagnetic field, respectively. In comparison to the SS-BHs, the LQG-BHs exhibit weaker oscillations and a slower decay rate during the intermediate time, primarily dominated by the fundamental mode. As expected, this observation aligns with the characteristics revealed by the fundamental mode presented in Tables I–IV. In the asymptotically late times, the quasinormal ringing is suppressed, and both LQG-BH and SS-BH follow the same power-law tail as $\Psi(t) \sim t^{-(2l+3)}$ [104–106].

In addition, we use the Prony method as described in [107] to calculate the fundamental mode. We will select the data from the time-domain profile during the intermediate time. We have presented the results for both the scalar field and electromagnetic field in Tables V and VI, respectively. These findings align with the outcomes obtained by directly solving the eigenvalue problem, as

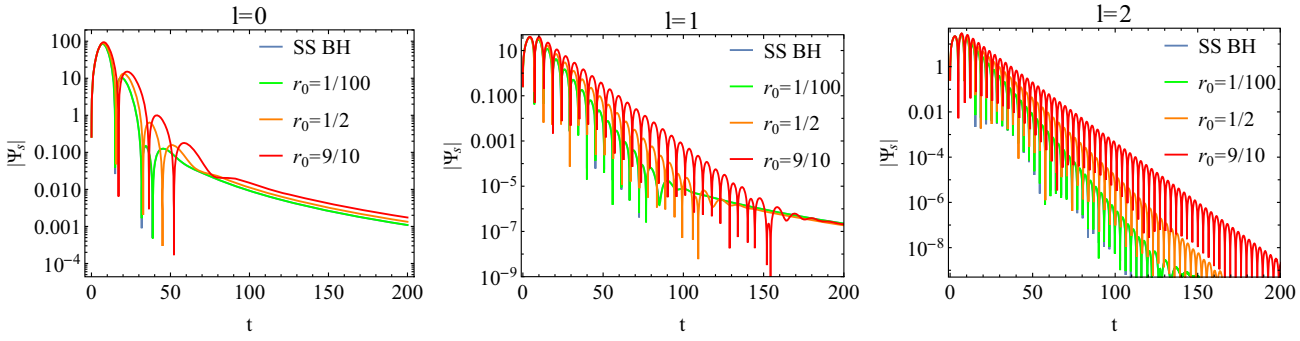

FIG. 9. The semilog plot of the time evolution of the scalar field $|\Psi_s(r)|$ for different r_0 with fixed l. Here, we have fixed the tortoise coordinate $r_* = 5$.

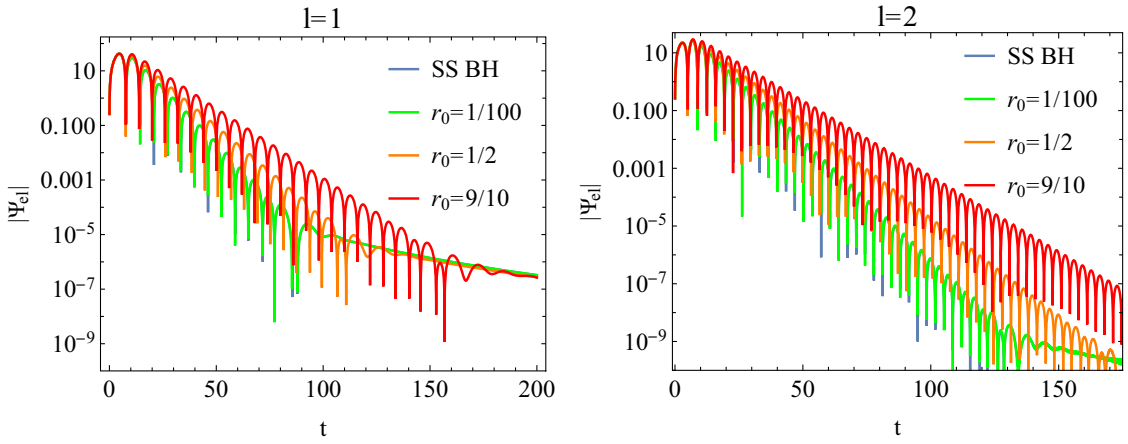

FIG. 10. The semilog plot of the time evolution of the electromagnetic field $|\Psi_{el}(r)|$ for different r_0 with fixed l. Here, we have fixed the tortoise coordinate $r_* = 5$.

presented in Tables I–IV. In theory, we can fit the higher overtone QNFs after subtracting the contribution of the fundamental mode if the quasinormal ringing stage is sufficiently prolonged. Nevertheless, in real-world applications, fitting the higher overtones can be challenging due to their rapid damping, causing them to become nearly indistinguishable from numerical errors. We intend to undertake this analysis in the near future.

TABLE V. The fundamental modes of the scalar field perturbation for various values of l and r_0, which are determined using the Prony method.

l	ω $(r_0 = 0)$	ω $(r_0 = 1/100)$	ω $(r_0 = 1/2)$	ω $(r_0 = 9/10)$
0	0.22114–0.21068i	0.22055–0.20984i	0.20155–0.16416i	0.17251–0.13331i
1	0.58588–0.19513i	0.58577–0.19443i	0.57966–0.15821i	0.57122–0.12296i

TABLE VI. The fundamental modes of the electromagnetic field perturbation for various values of l and r_0, which are determined using the Prony method.

l	ω $(r_0 = 0)$	ω $(r_0 = 1/100)$	ω $(r_0 = 1/2)$	ω $(r_0 = 9/10)$
1	0.49626–0.18372i	0.49660–0.18319i	0.51305–0.15239i	0.52317–0.11786i
2	0.91495–0.19021i	0.91516–0.18959i	0.92474–0.15566i	0.93038–0.12032i

VI. CONCLUSION AND DISCUSSION

With the rapid development of GW detection techniques, detection of the quantum gravity effect is expected. To extract substantial information from GW detectors, one must thoroughly know the main features and behaviors of the QNM for LQG-BHs. As the first step, we investigate the QNM for both the scalar field and the electromagnetic field over the covariant LQG-BH proposed in [55,56].

First, we focus on the fundamental modes. It is found that the system is always stable under scalar field or electromagnetic field perturbations, and the LQG effect results in faster decaying modes. The difference is that the LQG effect reduces the oscillations in the scalar field, however, it enhances oscillations in the electromagnetic field. In addition, we find that the system under the scalar field perturbation enjoys faster decaying modes with more oscillations than the electromagnetic field.

Some peculiar phenomena emerge in the QNM spectra with higher overtones. A noteworthy characteristic is the pronounced deviation observed in the first several overtones from their Schwarzschild counterparts, with this deviation increasing as the overtone number rises. Particularly noteworthy is the case of the scalar field with $l = 0$, where the real oscillation frequency of the second overtone decreases by more than 6 times its Schwarzschild limit, while the fundamental mode undergoes only minor changes. This observation is also reflected in the trajectory within the $\omega_R - |\omega_I|$ phase diagram, which spirals toward a stable point. This emergence of the outburst of overtones can be attributed to disparities in the region near the event horizon between the Schwarzschild BH and the LQG-corrected BH. Another notable phenomenon in higher overtones is the presence of oscillatory behavior in the QNFs of the scalar field with $l = 0$ as the quantum parameter r_0 experiences a significant increase. These oscillations become more pronounced with a higher overtone number. This oscillatory pattern may be associated with the extremal effect.

Finally, we note some open questions deserving further exploration.

(i) It would be interesting to extend our investigation to the Dirac field and see if the peculiar property still emerges in the QNM spectra.

(ii) It is definitely interesting and valuable to further study the QNM spectrum of the gravity perturbations. It provides us a platform for detecting quantum gravity effects using the GW detector. In addition, we can examine if the isospectrality still holds in this LQG-BH model.

(iii) In [108], the anomalous decay rate of QNMs of a massive scalar field is observed. Depending on how large the mass of the scalar field is, the decay timescales of the QNMs either grow or decay with increasing angular harmonic numbers. This anomalous behavior is seen in much larger class models beyond a simple massive scalar field; see Refs. [109–113] and references therein. It will be interesting to see how the LQG effect affects this anomalous behavior.

(iv) We can also construct an effective rotating LQG-BH solution using the Newman-Janis algorithm, starting with this spherical symmetric LQG-BH, and study the LQG effects on its QNM spectrum and shadow, allowing us to constrain the LQG parameters using the GW detector and the Event Horizon Telescope.

We plan to investigate these questions and publish our results in the near future.

ACKNOWLEDGMENTS

This work is supported by National Key R&D Program of China (No. 2020YFC2201400), the Natural Science Foundation of China under Grants No. 12375054 and No. 12375055, the Postgraduate Research and Practice Innovation Program of Jiangsu Province under Grant No. KYCX20_2973, the Postgraduate Scientific Research Innovation Project of Hunan Province under Grant No. CX20220509, the Science and Technology Planning Project of Guangzhou (202201010655), the Fok Ying Tung Education Foundation under Grant No. 171006, and the Natural Science Foundation of Jiangsu Province under Grant No. BK20211601. J.-P. W. is also supported by the Top Talent Support Program from Yangzhou University.

APPENDIX A: WAVE EQUATIONS

In this appendix, we will derive the wave equations for the scalar and electromagnetic fields in detail. First, we shall provide a generic version of the wave equation in a static spherically symmetric spacetime. The cases of scalar and electromagnetic fields are then discussed in detail.

Because the spacetime is static spherically symmetric, we can separate variables using the spherical function and write the radial equation in the form

$$\big(\mathcal{K}(r)\mathcal{S}(r)\hat{\Psi}'(r)\big)' + \left(\Lambda\mathcal{F}(r) + \mathcal{K}(r)\frac{\omega^2}{\mathcal{S}(r)}\right)\hat{\Psi}(r) = 0, \tag{A1}$$

where $\hat{\Psi}$ is the radial part of the wave function, the coefficient functions $\{\mathcal{K}, \mathcal{F}, \mathcal{S}\}$ only depend on the radial coordinate r, and Λ is the separation constant. After introducing the tortoise coordinate r_* and redefining the wave function as

$$\frac{dr_*}{dr} = \frac{1}{\mathcal{S}(r)}, \qquad \hat{\Psi}(r) = \frac{\Psi}{\sqrt{\mathcal{K}(r)}}, \tag{A2}$$

Eq. (A1) can be recast into the following form:

$$\frac{d^2\Psi(r_*)}{dr_*^2}+\left(\omega^2-V_{\rm eff}(r_*)\right)\Psi(r_*)=0. \tag{A3}$$

The above formula provides a general transformation from the usual wave equation to its Schrödinger-like counterpart.

In the following, we will go over the specific form of the wave equations for scalar and electromagnetic fields. For the scalar field equation, we perform the separation as $\Phi(t,r,\theta,\phi)=\sum_{l,m}\hat{\Psi}(r)e^{-i\omega t}Y_{lm}(\theta,\phi)$, where $Y_{lm}(\theta,\phi)$ are the spherical harmonics. When the particular form of the LQG-BH background (6) is substituted into the wave equation (A1), one obtains

$$\left(r^2f(r)\sqrt{g(r)}\hat{\Psi}'(r)\right)'+\left(\frac{r^2\omega^2}{f(r)\sqrt{g(r)}}-\frac{l(l+1)}{\sqrt{g(r)}}\right)\hat{\Psi}(r)=0. \tag{A4}$$

We can read off the coefficient functions by comparing Eq. (A4) to Eq. (A1),

$$\mathcal{K}(r)=r^2,\qquad \mathcal{S}=f(r)\sqrt{g(r)}. \tag{A5}$$

The Schrödinger-like version of the wave equation is then easily given as

$$\frac{\partial^2\Psi}{\partial r_*^2}+(\omega^2-V_s)\Psi=0, \tag{A6}$$

$$V_s=f(r)\frac{l(l+1)}{r^2}+\frac{1}{2r}\frac{d}{dr}f(r)^2g(r). \tag{A7}$$

For the electromagnetic field, we can expand the gauge field A_μ in vector spherical harmonics [114,115],

$$A_\mu(t,r,\theta,\phi)=\sum_{l,m}\left(\begin{bmatrix}0\\0\\\frac{a_{lm}(r)}{\sin\theta}\partial_\phi Y_{lm}\\-a_{lm}(r)\sin\theta\partial_\theta Y_{lm}\end{bmatrix}+\begin{bmatrix}p_{lm}(r)Y_{lm}\\h_{lm}(r)Y_{lm}\\k_{lm}(r)\partial_\theta Y_{lm}\\k_{lm}(r)\partial_\phi Y_{lm}\end{bmatrix}\right)e^{-i\omega t}, \tag{A8}$$

where the first term is the odd (axial) perturbation and second term is the even (polar) perturbation. Then, in the following, we will show how to derive the odd and the even perturbation equations.

When we switch on the odd electromagnetic field perturbation, we can explicitly write down the radial equation as

$$\left(f(r)\sqrt{g(r)}a'_{lm}(r)\right)'+\left(\frac{\omega^2}{f(r)\sqrt{g(r)}}-\frac{l(l+1)}{r^2\sqrt{g(r)}}\right)a_{lm}(r)=0. \tag{A9}$$

It is easy to find that $\mathcal{K}=1$ and $\mathcal{S}=f(r)\sqrt{g(r)}$. Thus, we have

$$V_{\rm odd}=f(r)\frac{l(l+1)}{r^2}, \tag{A10}$$

where $\Psi=a_{lm}(r)$.

For the even perturbation of the electromagnetic field, the radial equation becomes

$$\begin{aligned}&p''_{lm}(r)+q(r)p'_{lm}(r)+i\omega\left(h'_{lm}(r)+q(r)h_{lm}(r)\right)+\frac{l(l+1)}{r^2f(r)g(r)}\left(p_{lm}(r)+i\omega k_{lm}(r)\right)=0,\\&-i\omega p'_{lm}(r)+\omega^2h_{lm}(r)+\frac{l(l+1)}{r^2}f(r)\left(-h_{lm}(r)+k'_{lm}(r)\right)=0,\end{aligned} \tag{A11}$$

where $q(r)=\frac{2}{r}+\frac{g'(r)}{2g(r)}$. After introducing a new variable

$$\hat{\Psi}(r)=-p'_{lm}(r)-i\omega h_{lm}(r), \tag{A12}$$

Eq. (A11) can be reduced to

$$(r^4 f(r) g(r)^{3/2} \hat{\Psi}'(r))' + \left(\frac{r^4 \omega^2 \sqrt{g(r)}}{f(r)} - l(l+1) r^2 \sqrt{g(r) + \frac{1}{2} J(r)} \right) \hat{\Psi}(r) = 0, \tag{A13}$$

where $J(r) = r^2 \sqrt{g(r)} (r f'(r)(4g(r) + r g'(r)) + f(r) \times (4g(r) + r(6g'(r) + r g''(r))))$. Thus, the coefficient functions are $\mathcal{K} = r^4 \sqrt{g(r)}$ and $\mathcal{S} = f(r)\sqrt{g(r)}$ and then we have

$$V_{\text{even}} = f(r) \frac{l(l+1)}{r^2}. \tag{A14}$$

We find that the effective potentials for odd and even electromagnetic field perturbations are the same. Therefore, we will use V_{el} to signify the effective potential of the electromagnetic field rather than V_{odd} and V_{even}.

APPENDIX B: QNMs IN THE EIKONAL LIMIT

In this appendix, we will show the connection between the QNMs in the eikonal limit and the behavior of a null particle trapped on the unstable circular geodesic. For a null particle, the Lagrange is[1]

$$\mathcal{L}(x, \dot{x}) = 1/2 g_{\mu\nu} \dot{x}^\mu \dot{x}^\nu. \tag{B1}$$

We start with the spherically symmetric geometry (6). Thanks to the symmetry, one can only consider the geodesics in the equatorial plane: $\theta = \pi/2$. Then the Lagrangian (B1) becomes

$$2\mathcal{L} = -f(r)\dot{t}^2 + \frac{\dot{r}^2}{f(r)g(r)} + r^2 \dot{\phi}^2, \tag{B2}$$

where the dot represents the derivative with respect to the affine parameter τ. In this system, there are two constants of the motion, which are

$$P_t = -f(r)\dot{t} = -E, \qquad P_\phi = r^2 \dot{\phi} = L. \tag{B3}$$

Using the canonical transform and combining the above equations (B2) and (B3), we have the following reduced Hamiltonian system:

$$2\mathcal{H} = E\dot{t} + \frac{\dot{r}^2}{f(r)g(r)} + L\dot{\phi}. \tag{B4}$$

Since the Hamiltonian $\mathcal{H}$ satisfies the constraint $\mathcal{H} = 0$, we have

$$\dot{r}^2 + V_{\text{eff}} = 0, \tag{B5}$$

where the effective potential is

$$V_{\text{eff}} = g(r) \left(\frac{L^2}{r^2} f(r) - E^2 \right). \tag{B6}$$

Because $\dot{r}^2 > 0$, the photon can only emerge in the area of negative potential. When the angular momentum is small, the photon will fall from infinity into the black hole. However, for the large angular momentum, the photon will escape the bondage of the black hole and go back to infinity. Therefore, the critical circular orbit for the photon can be derived from the unstable conditions

$$V_{\text{eff}} = 0, \qquad \frac{\partial V_{\text{eff}}}{\partial r} = 0, \qquad \frac{\partial^2 V_{\text{eff}}}{\partial r^2} < 0. \tag{B7}$$

From the above conditions, we can obtain the equation for the critical radius r_c,

$$2 f_c(r) = r_c f_c'(r). \tag{B8}$$

Correspondingly, we have the critical impact parameters b_c,

$$b_c = \frac{L}{E} = \frac{r_c}{\sqrt{f_c(r)}}. \tag{B9}$$

Then, the shadow radius R_s and Lyapunov exponents λ can be calculated as follows:

$$R_s = \sqrt{\zeta^2 + \eta^2} = b_c = 3\sqrt{3} m, \tag{B10}$$

$$\lambda = \sqrt{\frac{V_{\text{eff}}''}{2\dot{t}^2}} = \sqrt{-\frac{r_c^2}{f(r_c)} \left(\frac{d^2}{dr_*^2} \frac{f(r)}{r^2} \right) \Big|_{r=rc}}, \tag{B11}$$

where $\{\zeta, \eta\}$ are the celestial coordinates. We find that the shadow radius reduces to the one of the SS-BH [118,119]. This means that the LQG effect does not change the shape of the shadow. However, the LQG correction affects the Lyapunov exponent λ.

On the other hand, we shall use the first order WKB approximation to obtain the analytic form of the QNMs in the eikonal limit ($l \to \infty$). In this limit, the last term of the effective potential (16) can be ignored, resulting in the following form of the effective potential:

$$V_\infty(r) = f(r) \frac{l^2}{r^2}. \tag{B12}$$

[1]For the calculation details of the geodesic of a null particle, please refer to [89,90,116,117].

Remembering that the potentials (B6) and (B12) are the same, therefore, in the eikonal limit, the QNMs may be obtained by the multiples of the frequency and the instability timescale of the unstable circular null geodesic [89],

$$\omega = \Omega_c l - i\left(n + \frac{1}{2}\right)|\lambda|, \tag{B13}$$

where Ω_c is the angular velocity and can be worked out as

$$\Omega_c = \frac{\dot{\phi}}{\dot{t}} = \frac{1}{b_c}. \tag{B14}$$

[1] C. Rovelli, *Quantum Gravity* (Cambridge University Press, Cambridge, England, 2004).
[2] T. Thiemann, Modern canonical quantum general relativity, arXiv:gr-qc/0110034.
[3] A. Ashtekar and J. Lewandowski, Background independent quantum gravity: A status report, Classical Quantum Gravity **21**, R53 (2004).
[4] M. Han, W. Huang, and Y. Ma, Fundamental structure of loop quantum gravity, Int. J. Mod. Phys. D **16**, 1397 (2007).
[5] M. Bojowald, Absence of singularity in loop quantum cosmology, Phys. Rev. Lett. **86**, 5227 (2001).
[6] A. Ashtekar, T. Pawlowski, and P. Singh, Quantum nature of the big bang, Phys. Rev. Lett. **96**, 141301 (2006).
[7] A. Ashtekar, T. Pawlowski, and P. Singh, Quantum nature of the big bang: An analytical and numerical investigation. I., Phys. Rev. D **73**, 124038 (2006).
[8] A. Ashtekar, T. Pawlowski, and P. Singh, Quantum nature of the big bang: Improved dynamics, Phys. Rev. D **74**, 084003 (2006).
[9] A. Ashtekar, M. Bojowald, and J. Lewandowski, Mathematical structure of loop quantum cosmology, Adv. Theor. Math. Phys. **7**, 233 (2003).
[10] M. Bojowald, Loop quantum cosmology, Living Rev. Relativity **8**, 11 (2005).
[11] A. Ashtekar and P. Singh, Loop quantum cosmology: A status report, Classical Quantum Gravity **28**, 213001 (2011).
[12] E. Wilson-Ewing, Testing loop quantum cosmology, C.R. Phys. **18**, 207 (2017).
[13] V. Taveras, Corrections to the Friedmann equations from LQG for a universe with a free scalar field, Phys. Rev. D **78**, 064072 (2008).
[14] Y. Ding, Y. Ma, and J. Yang, Effective scenario of loop quantum cosmology, Phys. Rev. Lett. **102**, 051301 (2009).
[15] J. Yang, Y. Ding, and Y. Ma, Alternative quantization of the Hamiltonian in loop quantum cosmology II: Including the Lorentz term, Phys. Lett. B **682**, 1 (2009).
[16] M. Bojowald and A. Tsobanjan, Effective constraints for relativistic quantum systems, Phys. Rev. D **80**, 125008 (2009).
[17] M. Bojowald and A. Tsobanjan, Effective constraints and physical coherent states in quantum cosmology: A numerical comparison, Classical Quantum Gravity **27**, 145004 (2010).
[18] M. Bojowald, D. Brizuela, H. H. Hernandez, M. J. Koop, and H. A. Morales-Tecotl, High-order quantum backreaction and quantum cosmology with a positive cosmological constant, Phys. Rev. D **84**, 043514 (2011).
[19] A. Ashtekar, M. Campiglia, and A. Henderson, Loop quantum cosmology and spin foams, Phys. Lett. B **681**, 347 (2009).
[20] A. Ashtekar, M. Campiglia, and A. Henderson, Casting loop quantum cosmology in the spin foam paradigm, Classical Quantum Gravity **27**, 135020 (2010).
[21] A. Ashtekar, M. Campiglia, and A. Henderson, Path integrals and the WKB approximation in loop quantum cosmology, Phys. Rev. D **82**, 124043 (2010).
[22] H. Huang, Y. Ma, and L. Qin, Path integral and effective Hamiltonian in loop quantum cosmology, Gen. Relativ. Gravit. **45**, 1191 (2013).
[23] L. Qin, G. Deng, and Y.-G. Ma, Path integrals and alternative effective dynamics in loop quantum cosmology, Commun. Theor. Phys. **57**, 326 (2012).
[24] L. Qin and Y. Ma, Coherent state functional integrals in quantum cosmology, Phys. Rev. D **85**, 063515 (2012).
[25] L. Qin and Y. Ma, Coherent state functional integral in loop quantum cosmology: Alternative dynamics, Mod. Phys. Lett. A **27**, 1250078 (2012).
[26] M. Bojowald, G. Date, and K. Vandersloot, Homogeneous loop quantum cosmology: The role of the spin connection, Classical Quantum Gravity **21**, 1253 (2004).
[27] P. Singh and A. Toporensky, Big crunch avoidance in $K = 1$ semiclassical loop quantum cosmology, Phys. Rev. D **69**, 104008 (2004).
[28] G. V. Vereshchagin, Qualitative approach to semi-classical loop quantum cosmology, J. Cosmol. Astropart. Phys. 07 (2004) 013.
[29] G. Date, Absence of the Kasner singularity in the effective dynamics from loop quantum cosmology, Phys. Rev. D **71**, 127502 (2005).
[30] G. Date and G. M. Hossain, Genericness of a big bounce in isotropic loop quantum cosmology, Phys. Rev. Lett. **94**, 011302 (2005).

[31] R. Goswami, P. S. Joshi, and P. Singh, Quantum evaporation of a naked singularity, Phys. Rev. Lett. **96**, 031302 (2006).
[32] M. Bojowald, The early Universe in loop quantum cosmology, J. Phys. Conf. Ser. **24**, 77 (2005).
[33] T. Stachowiak and M. Szydlowski, Exact solutions in bouncing cosmology, Phys. Lett. B **646**, 209 (2007).
[34] A. Ashtekar and M. Bojowald, Quantum geometry and the Schwarzschild singularity, Classical Quantum Gravity **23**, 391 (2006).
[35] L. Modesto, Loop quantum black hole, Classical Quantum Gravity **23**, 5587 (2006).
[36] L. Modesto, Semiclassical loop quantum black hole, Int. J. Theor. Phys. **49**, 1649 (2010).
[37] M. Campiglia, R. Gambini, and J. Pullin, Loop quantization of spherically symmetric midi-superspaces, Classical Quantum Gravity **24**, 3649 (2007).
[38] M. Bojowald and S. Brahma, Signature change in two-dimensional black-hole models of loop quantum gravity, Phys. Rev. D **98**, 026012 (2018).
[39] C. G. Boehmer and K. Vandersloot, Loop quantum dynamics of the Schwarzschild interior, Phys. Rev. D **76**, 104030 (2007).
[40] D.-W. Chiou, Phenomenological loop quantum geometry of the Schwarzschild black hole, Phys. Rev. D **78**, 064040 (2008).
[41] D.-W. Chiou, Phenomenological dynamics of loop quantum cosmology in Kantowski-Sachs spacetime, Phys. Rev. D **78**, 044019 (2008).
[42] A. Joe and P. Singh, Kantowski-Sachs spacetime in loop quantum cosmology: Bounds on expansion and shear scalars and the viability of quantization prescriptions, Classical Quantum Gravity **32**, 015009 (2015).
[43] J. Yang, C. Zhang, and Y. Ma, Loop quantum black hole in a gravitational collapse model, Eur. Phys. J. C **83**, 619 (2023).
[44] W.-C. Gan, X.-M. Kuang, Z.-H. Yang, Y. Gong, A. Wang, and B. Wang, Non-existence of quantum black hole horizons in the improved dynamics approach, arXiv:2212.14535.
[45] A. Corichi, T. Vukasinac, and J. A. Zapata, Polymer quantum mechanics and its continuum limit, Phys. Rev. D **76**, 044016 (2007).
[46] A. Corichi and P. Singh, Loop quantization of the Schwarzschild interior revisited, Classical Quantum Gravity **33**, 055006 (2016).
[47] J. Olmedo, S. Saini, and P. Singh, From black holes to white holes: A quantum gravitational, symmetric bounce, Classical Quantum Gravity **34**, 225011 (2017).
[48] A. Ashtekar, J. Olmedo, and P. Singh, Quantum transfiguration of Kruskal black holes, Phys. Rev. Lett. **121**, 241301 (2018).
[49] A. Ashtekar, J. Olmedo, and P. Singh, Quantum extension of the Kruskal spacetime, Phys. Rev. D **98**, 126003 (2018).
[50] R. Gambini, J. Olmedo, and J. Pullin, Spherically symmetric loop quantum gravity: Analysis of improved dynamics, Classical Quantum Gravity **37**, 205012 (2020).
[51] J. G. Kelly, R. Santacruz, and E. Wilson-Ewing, Effective loop quantum gravity framework for vacuum spherically symmetric spacetimes, Phys. Rev. D **102**, 106024 (2020).
[52] V. Husain, J. G. Kelly, R. Santacruz, and E. Wilson-Ewing, Fate of quantum black holes, Phys. Rev. D **106**, 024014 (2022).
[53] M. Han and H. Liu, Covariant $\bar{\mu}$-scheme effective dynamics, mimetic gravity, and non-singular black holes: Applications to spherical symmetric quantum gravity and CGHS model, arXiv:2212.04605.
[54] A. Alonso-Bardaji and D. Brizuela, Anomaly-free deformations of spherical general relativity coupled to matter, Phys. Rev. D **104**, 084064 (2021).
[55] A. AlonsoBardaji, D. Brizuela, and R. Vera, An effective model for the quantum Schwarzschild black hole, Phys. Lett. B **829**, 137075 (2022).
[56] A. AlonsoBardaji, D. Brizuela, and R. Vera, Nonsingular spherically symmetric black-hole model with holonomy corrections, Phys. Rev. D **106**, 024035 (2022).
[57] E. Berti, V. Cardoso, and A. O. Starinets, Quasinormal modes of black holes and black branes, Classical Quantum Gravity **26**, 163001 (2009).
[58] B. F. Schutz and C. M. Will, Black hole normal modes—A semianalytic approach, Astrophys. J. Lett. **291**, L33 (1985).
[59] S. Iyer and C. M. Will, Black hole normal modes: A WKB approach. 1. Foundations and application of a higher order WKB analysis of potential barrier scattering, Phys. Rev. D **35**, 3621 (1987).
[60] J. W. Guinn, C. M. Will, Y. Kojima, and B. F. Schutz, High overtone normal modes of Schwarzschild black holes, Classical Quantum Gravity **7**, L47 (1990).
[61] R. A. Konoplya, Quasinormal modes of the Schwarzschild black hole and higher order WKB approach, J. Phys. Stud. **8**, 93 (2004).
[62] R. A. Konoplya, Quasinormal behavior of the *D*-dimensional Schwarzschild black hole and higher order WKB approach, Phys. Rev. D **68**, 024018 (2003).
[63] J. Matyjasek and M. Opala, Quasinormal modes of black holes. The improved semianalytic approach, Phys. Rev. D **96**, 024011 (2017).
[64] G. T. Horowitz and V. E. Hubeny, Quasinormal modes of AdS black holes and the approach to thermal equilibrium, Phys. Rev. D **62**, 024027 (2000).
[65] E. W. Leaver, An analytic representation for the quasi normal modes of Kerr black holes, Proc. R. Soc. A **402**, 285 (1985).
[66] H. Ciftci, R. L. Hall, and N. Saad, Perturbation theory in a framework of iteration methods, Phys. Lett. A **340**, 388 (2005).
[67] H. T. Cho, A. S. Cornell, J. Doukas, and W. Naylor, Black hole quasinormal modes using the asymptotic iteration method, Classical Quantum Gravity **27**, 155004 (2010).
[68] H. T. Cho, A. S. Cornell, J. Doukas, T. R. Huang, and W. Naylor, A new approach to black hole quasinormal modes: A review of the asymptotic iteration method, Adv. Theor. Math. Phys. **2012**, 281705 (2012).
[69] J. P. Boyd, *Chebyshev & Fourier Spectral Methods* (Courier Dover Publications, New York, 2000).
[70] A. Jansen, Overdamped modes in Schwarzschild–de Sitter and a Mathematica package for the numerical computation of quasinormal modes, Eur. Phys. J. Plus **132**, 546 (2017).

[71] J.-P. Wu and P. Liu, Quasi-normal modes of holographic system with Weyl correction and momentum dissipation, Phys. Lett. B **780**, 616 (2018).
[72] G. Fu and J.-P. Wu, EM duality and quasinormal modes from higher derivatives with homogeneous disorder, Adv. High Energy Phys. **2019**, 5472310 (2019).
[73] G. Fu, D. Zhang, P. Liu, X.-M. Kuang, Q. Pan, and J.-P. Wu, Quasi-normal modes and Hawking radiation of a charged Weyl black hole, Phys. Rev. D **107**, 044049 (2023).
[74] W. Xiong, P. Liu, C.-Y. Zhang, and C. Niu, Quasi-normal modes of the Einstein-Maxwell-aether black hole, Phys. Rev. D **106**, 064057 (2022).
[75] P. Liu, C. Niu, and C.-Y. Zhang, Linear instability of charged massless scalar perturbation in regularized 4D charged Einstein-Gauss-Bonnet anti de-Sitter black holes, Chin. Phys. C **45**, 025111 (2021).
[76] P. Liu, C. Niu, and C.-Y. Zhang, Instability of regularized 4D charged Einstein-Gauss-Bonnet de-Sitter black holes, Chin. Phys. C **45**, 025104 (2021).
[77] J. L. Jaramillo, R. Panosso Macedo, and L. Al Sheikh, Pseudospectrum and black hole quasinormal mode instability, Phys. Rev. X **11**, 031003 (2021).
[78] J. L. Jaramillo, R. Panosso Macedo, and L. A. Sheikh, Gravitational wave signatures of black hole quasi-normal mode instability, Phys. Rev. Lett. **128**, 211102 (2022).
[79] K. Destounis, R. P. Macedo, E. Berti, V. Cardoso, and J. L. Jaramillo, Pseudospectrum of Reissner-Nordström black holes: Quasinormal mode instability and universality, Phys. Rev. D **104**, 084091 (2021).
[80] L. A. H. Mamani, A. D. D. Masa, L. T. Sanches, and V. T. Zanchin, Revisiting the quasinormal modes of the Schwarzschild black hole: Numerical analysis, Eur. Phys. J. C **82**, 897 (2022).
[81] E. Berti and K. D. Kokkotas, Asymptotic quasinormal modes of Reissner-Nordström and Kerr black holes, Phys. Rev. D **68**, 044027 (2003).
[82] R. A. Konoplya, A. F. Zinhailo, J. Kunz, Z. Stuchlik, and A. Zhidenko, Quasinormal ringing of regular black holes in asymptotically safe gravity: The importance of overtones, J. Cosmol. Astropart. Phys. 10 (2022) 091.
[83] R. A. Konoplya and A. Zhidenko, First few overtones probe the event horizon geometry, arXiv:2209.00679.
[84] R. A. Konoplya, Quasinormal modes in higher-derivative gravity: Testing the black hole parametrization and sensitivity of overtones, Phys. Rev. D **107**, 064039 (2023).
[85] R. A. Konoplya, Quasinormal modes and grey-body factors of regular black holes with a scalar hair from the effective field theory, J. Cosmol. Astropart. Phys. 07 (2023) 001.
[86] R. A. Konoplya, D. Ovchinnikov, and B. Ahmedov, Bardeen spacetime as a quantum corrected Schwarzschild black hole: Quasinormal modes and Hawking radiation, Phys. Rev. D **108**, 104054 (2023).
[87] Z. S. Moreira, H. C. D. Lima Junior, L. C. B. Crispino, and C. A. R. Herdeiro, Quasinormal modes of a holonomy corrected Schwarzschild black hole, Phys. Rev. D **107**, 104016 (2023).
[88] J. Jing and Q. Pan, Quasinormal modes and second order thermodynamic phase transition for Reissner-Nordström black hole, Phys. Lett. B **660**, 13 (2008).
[89] V. Cardoso, A. S. Miranda, E. Berti, H. Witek, and V. T. Zanchin, Geodesic stability, Lyapunov exponents and quasinormal modes, Phys. Rev. D **79**, 064016 (2009).
[90] S.-W. Wei and Y.-X. Liu, Null geodesics, quasinormal modes, and thermodynamic phase transition for charged black holes in asymptotically flat and dS spacetimes, Chin. Phys. C **44**, 115103 (2020).
[91] K. Jusufi, Quasinormal modes of black holes surrounded by dark matter and their connection with the shadow radius, Phys. Rev. D **101**, 084055 (2020).
[92] H. Guo, H. Liu, X.-M. Kuang, and B. Wang, Acoustic black hole in Schwarzschild spacetime: Quasinormal modes, analogous Hawking radiation, and shadows, Phys. Rev. D **102**, 124019 (2020).
[93] C. Liu, T. Zhu, Q. Wu, K. Jusufi, M. Jamil, M. Azreg-Aïnou, and A. Wang, Shadow and quasinormal modes of a rotating loop quantum black hole, Phys. Rev. D **101**, 084001 (2020); **103**, 089902(E) (2021).
[94] R. Ling, H. Guo, H. Liu, X.-M. Kuang, and B. Wang, Shadow and near-horizon characteristics of the acoustic charged black hole in curved spacetime, Phys. Rev. D **104**, 104003 (2021).
[95] L. Bombelli and E. Calzetta, Chaos around a black hole, Classical Quantum Gravity **9**, 2573 (1992).
[96] N. J. Cornish and J. J. Levin, Lyapunov timescales and black hole binaries, Classical Quantum Gravity **20**, 1649 (2003).
[97] K. Lin and W.-L. Qian, Echoes in star quasinormal modes using an alternative finite difference method, Chin. Phys. C **47**, 085101 (2023).
[98] Z. Zhu, S.-J. Zhang, C. E. Pellicer, B. Wang, and E. Abdalla, Stability of Reissner-Nordström black hole in de Sitter background under charged scalar perturbation, Phys. Rev. D **90**, 044042 (2014); **90**, 049904(A) (2014).
[99] E. Abdalla, C. E. Pellicer, J. de Oliveira, and A. B. Pavan, Phase transitions and regions of stability in Reissner-Nordström holographic superconductors, Phys. Rev. D **82**, 124033 (2010).
[100] Z.-H. Yang, G. Fu, X.-M. Kuang, and J.-P. Wu, Instability of de-Sitter black hole with massive scalar field coupled to Gauss-Bonnet invariant and the scalarized black holes, Eur. Phys. J. C **82**, 868 (2022).
[101] B. P. Abbott *et al.* (LIGO Scientific and Virgo Collaborations), Observation of gravitational waves from a binary black hole merger, Phys. Rev. Lett. **116**, 061102 (2016).
[102] R. A. Konoplya and A. Zhidenko, Quasinormal modes of black holes: From astrophysics to string theory, Rev. Mod. Phys. **83**, 793 (2011).
[103] K. D. Kokkotas and B. G. Schmidt, Quasinormal modes of stars and black holes, Living Rev. Relativity **2**, 2 (1999).
[104] C. Gundlach, R. H. Price, and J. Pullin, Late time behavior of stellar collapse and explosions: 1. Linearized perturbations, Phys. Rev. D **49**, 883 (1994).
[105] R. H. Price, Nonspherical perturbations of relativistic gravitational collapse. II. Integer-spin, zero-rest-mass fields, Phys. Rev. D **5**, 2439 (1972).
[106] R. H. Price, Nonspherical perturbations of relativistic gravitational collapse. 1. Scalar and gravitational perturbations, Phys. Rev. D **5**, 2419 (1972).

[107] A. Zhidenko, Linear perturbations of black holes: Stability, quasi-normal modes and tails, Ph.D. thesis, Sao Paulo University, 2009, arXiv:0903.3555.
[108] M. Lagos, P. G. Ferreira, and O. J. Tattersall, Anomalous decay rate of quasinormal modes, Phys. Rev. D **101**, 084018 (2020).
[109] A. Aragón, P. A. González, E. Papantonopoulos, and Y. Vásquez, Anomalous decay rate of quasinormal modes in Schwarzschild-dS and Schwarzschild-AdS black holes, J. High Energy Phys. 08 (2020) 120.
[110] A. Aragón, R. Bécar, P. A. González, and Y. Vásquez, Massive Dirac quasinormal modes in Schwarzschild–de Sitter black holes: Anomalous decay rate and fine structure, Phys. Rev. D **103**, 064006 (2021).
[111] R. D. B. Fontana, P. A. González, E. Papantonopoulos, and Y. Vásquez, Anomalous decay rate of quasinormal modes in Reissner-Nordström black holes, Phys. Rev. D **103**, 064005 (2021).
[112] P. A. González, E. Papantonopoulos, J. Saavedra, and Y. Vásquez, Quasinormal modes for massive charged scalar fields in Reissner-Nordström dS black holes: Anomalous decay rate, J. High Energy Phys. 06 (2022) 150.
[113] P. A. González, E. Papantonopoulos, A. Rincón, and Y. Vásquez, Quasinormal modes of massive scalar fields in four-dimensional wormholes: Anomalous decay rate, Phys. Rev. D **106**, 024050 (2022).
[114] C. DeWitt and B. S. DeWitt, in *Black Holes: les Astres Occlus* (Gordon and Breach Science Publishers, New York, 1972).
[115] V. Cardoso, Quasinormal modes and gravitational radiation in black hole spacetimes, other thesis, Lisbon, IST, 2003.
[116] S. Chandrasekhar, *The Mathematical Theory of Black Holes* (Oxford University Press, New York, 1986).
[117] V. Perlick, O. Y. Tsupko, and G. S. Bisnovatyi-Kogan, Influence of a plasma on the shadow of a spherically symmetric black hole, Phys. Rev. D **92**, 104031 (2015).
[118] H.-J. Blome and B. Mashhoon, Quasi-normal oscillations of a Schwarzschild black hole, Phys. Lett. **110A**, 231 (1984).
[119] M. S. Churilova, Analytical quasinormal modes of spherically symmetric black holes in the eikonal regime, Eur. Phys. J. C **79**, 629 (2019).